NANO LETTERS

pubs.acs.org/NanoLett Letter

# Fabrication-Aware Training for Two-Photon Polymerized Diffractive Deep Neural Networks

Jiale Yao,[▽] Jiabin Bi,[▽] Yuhang Xue, Liqun Xu, Zhaohui Ye, Haowen Liu, Bowen Chen, Jincheng Ni, Jiawen Li, Dong Wu, and Yanlei Hu*

Cite This: https://doi.org/10.1021/acs.nanolett.6c01607 Read Online



**ABSTRACT:** Diffractive deep neural networks (D2NNs) provide a promising pathway toward high-speed, energy-efficient optical computing. However, a substantial discrepancy between simulation and experiment remains when devices are fabricated by two-photon polymerization (TPP) for visible/near-infrared operation. This discrepancy is primarily due to fabrication constraints. In particular, the finite voxel size of the writing focus and the layer-by-layer slicing quantization attenuate high-spatial-frequency phase features and distort the designed wavefront. Here, a fabrication-aware training (FAT) strategy is introduced to incorporate these dominant constraints into the optimization loop through a differentiable model, thereby improving the experimental performance of two-photon polymerized D2NNs. In a handwritten digit recognition task, FAT increases the average experimental energy concentration ratio (ECR) from 6.15% to 11.50%. This reduces the simulation-to-experiment discrepancy by 79.03% while preserving the classification accuracy. These results demonstrate that fabrication-aware optimization substantially improves the functional fidelity of micro/nanoscale diffractive optical computing devices.

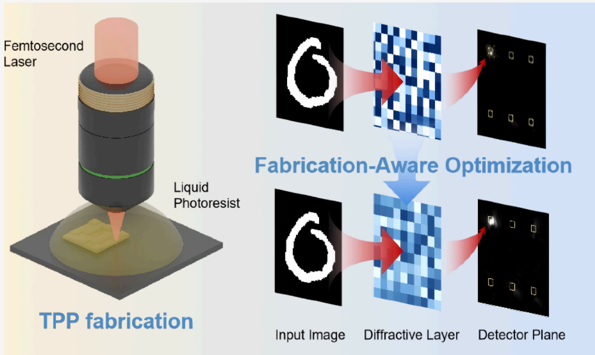


**KEYWORDS:** *two-photon polymerization, fabrication-aware training, diffractive deep neural networks*

Artificial intelligence (AI) has profoundly transformed modern information processing, while the escalating demand for throughput and energy efficiency is pushing conventional electronic hardware toward physical limits.[1−4] Optical neural networks (ONNs) have therefore attracted increasing interest by leveraging the inherent parallelism and ultralow latency of light.[5−9] Among ONN architectures, diffractive deep neural networks (D2NNs) perform inference and other computational tasks through passive diffractive layers that sculpt the optical wavefront.[10−14] These diffractive layers require no active power during operation, although optical illumination and detection remain necessary at the system level.

Initial demonstrations of D2NNs take place largely at terahertz wavelengths, where millimeter-scale features ease fabrication.[15−18] However, practical deployment with compact imaging optics favors visible or near-infrared operation. This shift drives diffractive features into the micro/nanoscale regime and increases manufacturing difficulty.[19−22] Two-photon polymerization (TPP) has emerged as a key enabling technology, providing three-dimensional, submicrometer-resolution laser lithography.[23,24] By writing voxel-by-voxel in a photoresist, TPP realizes dense three-dimensional diffractive structures suitable for compact D2NNs.

Despite the high nominal resolution associated with TPP, a pronounced discrepancy persists between idealized simulated designs and experimentally fabricated D2NNs. Standard training typically assumes continuous phase modulation and perfect geometric fidelity.[25,26] In practice, TPP imposes strong realizability constraints. The finite lateral extent of the focal volume acts as a spatial low-pass filter. Additionally, layer-by-layer writing discretizes the continuous height profile into axial steps.[27,28] These constraints induce phase errors during the physical realization, resulting in defocus, elevated background noise, and reduced energy concentration.

Previous studies have shown that such discrepancies can be addressed at different stages of the design−fabrication chain. Wang et al. related laser power, scanning speed, hatching distance, and slicing distance to the printed geometry through a lumped TPL process model, enabling Dammann gratings with diffraction performance approaching the theoretical limit.[29] This work demonstrates that fabrication should be

**Received:** April 2, 2026
**Revised:** August 20, 2026
**Accepted:** August 24, 2026

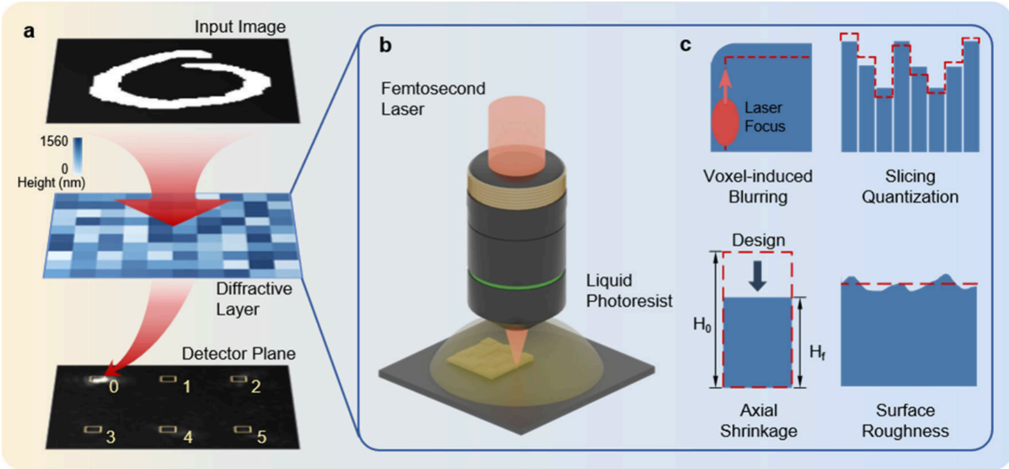


**Figure 1.** Conceptual overview of diffractive neural network operation, fabrication, and fabrication-induced perturbations. (a) Optical inference process, where the diffractive layer modulates the incident wavefront to route optical energy to class-specific detector regions. (b) TPP fabrication of the diffractive microstructure using a femtosecond laser in liquid photoresist. (c) Representative fabrication-induced effects, including voxel-induced blurring, slicing quantization, axial shrinkage, and surface roughness.

treated as a parameter-dependent transfer process that can be characterized and optimized, rather than as an unspecified resolution limit. Pan et al. evaluated the effects of corner rounding, height-profile smoothing, and polymer shrinkage in 3D-printed multilayer metalenses.[30] Moderate geometric approximation preserved the focal position and width, whereas the loss of fine height features produced a pronounced reduction in focusing efficiency, indicating that fabrication errors can affect energy concentration more strongly than coarse focal characteristics. At the optical-system level, Wu et al. corrected wide-angle projection distortion by mapping the intrinsic spherical wavefront to the desired Cartesian target before DOE design.[31] Although this approach addresses deterministic propagation geometry rather than fabrication error, it demonstrates that a known physical transformation can be incorporated upstream into the design process.

For diffractive neural networks, related approaches have introduced stochastic positional perturbations to improve misalignment tolerance,[32] engineered neuron geometries to enhance visible-wavelength modulation fidelity,[33] and incorporated measured physical responses through hybrid or in-situ training.[34−37] Collectively, these studies establish a common principle: reliable diffractive devices require the relevant physical nonidealities to be considered during calibration, design, or training. However, the finite writing voxel and discrete axial slicing of TPP have not been jointly embedded into the optimization of a task-specific D2NN height profile. FAT addresses this gap by evaluating slicing-compatible discrete heights during forward propagation and using TV regularization to reduce dependence on local height variations that are particularly susceptible to voxel-induced smoothing. It therefore complements process calibration and system-level precompensation by directing the optimization toward phase profiles that preserve task-relevant optical interference while being more faithfully realizable by TPP.

Here, we propose a fabrication-aware training (FAT) strategy to systematically bridge the discrepancy between simulation and experiment in TPP-fabricated D2NNs. Using a handwritten digit recognition task as a benchmark, a quantitative sensitivity analysis identifies voxel-induced blurring and slicing-induced height quantization as the dominant contributors to experimental performance loss. In contrast, axial shrinkage and surface roughness play secondary roles. Motivated by these findings, FAT integrates voxel-induced blurring and slicing quantization directly into the forward model. This physics-grounded optimization guides the network toward phase profiles that retain their intended optical functionality after fabrication. Experiments confirm that FAT substantially improves energy concentration and inference fidelity, providing a scalable route to robust micro/nanoscale diffractive ONNs.

To reduce the discrepancy between simulation and experiment, we first identify the dominant physical mechanisms responsible for performance degradation in TPP-fabricated diffractive networks. As summarized in Figure 1, this analysis is grounded in the operation principle of D2NNs, the TPP fabrication route, and the representative fabrication-induced effects considered in this work. We then establish a quantitative diagnostic framework and evaluate the sensitivity of inference performance to four representative fabrication-induced effects: voxel-induced blurring, slicing quantization, axial shrinkage, and surface roughness.

Rather than retraining for each error source, we apply each fabrication perturbation independently to the phase profile of a pretrained ideal baseline (termed the Naive model, which is designed for a handwritten digit recognition task using the MNIST dataset) and compute the resulting optical response by forward propagation. This procedure isolates the impact of each physical effect on the designed wavefront, enabling a direct comparison of their relative impact on inference performance.

The mathematical definitions of the four perturbation models are provided in the Supporting Information, together with representative output intensity distributions in Figures S2−S5. The parameter sweeps were selected to cover representative operating regimes encountered in high-resolution TPP fabrication. The voxel-blurring range represents the progressive lateral smoothing associated with the finite writing focus, whereas the quantization sweep spans axial discretization from finely sampled height profiles to only a few available height levels. The shrinkage and roughness ranges represent uniform axial contraction and stochastic local height variations,




https://doi.org/10.1021/acs.nanolett.6c01607
Nano Lett. XXXX, XXX, XXX−XXX

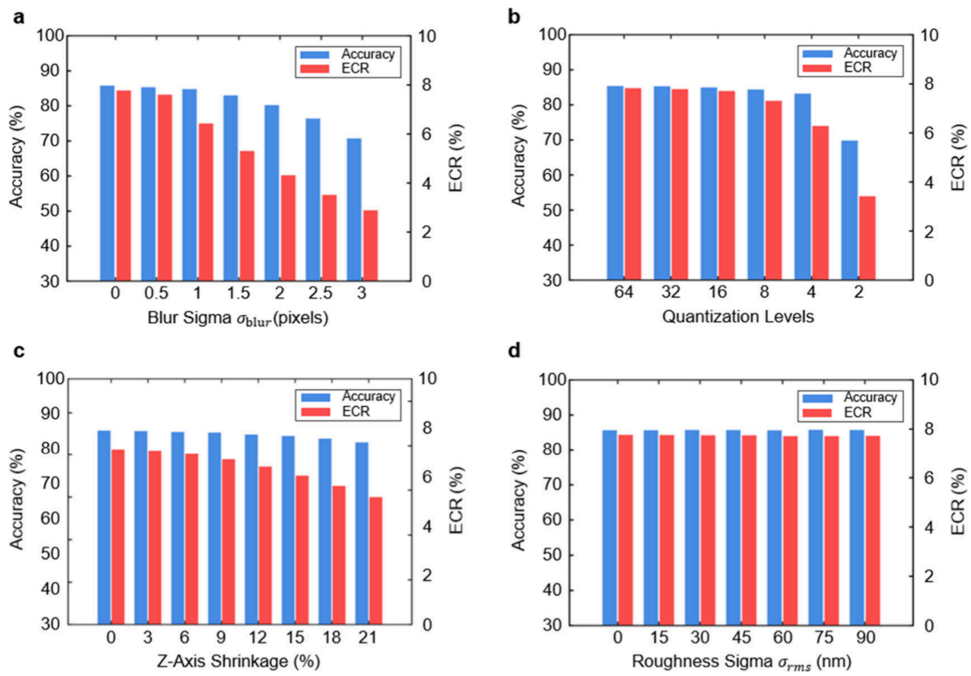


**Figure 2.** Sensitivity of the Naive model to representative TPP fabrication-induced errors. (a) Voxel-induced blurring. (b) Axial slicing quantization. (c) Axial shrinkage. (d) Surface roughness. Classification accuracy and energy concentration ratio (ECR) are shown in blue and red, respectively.

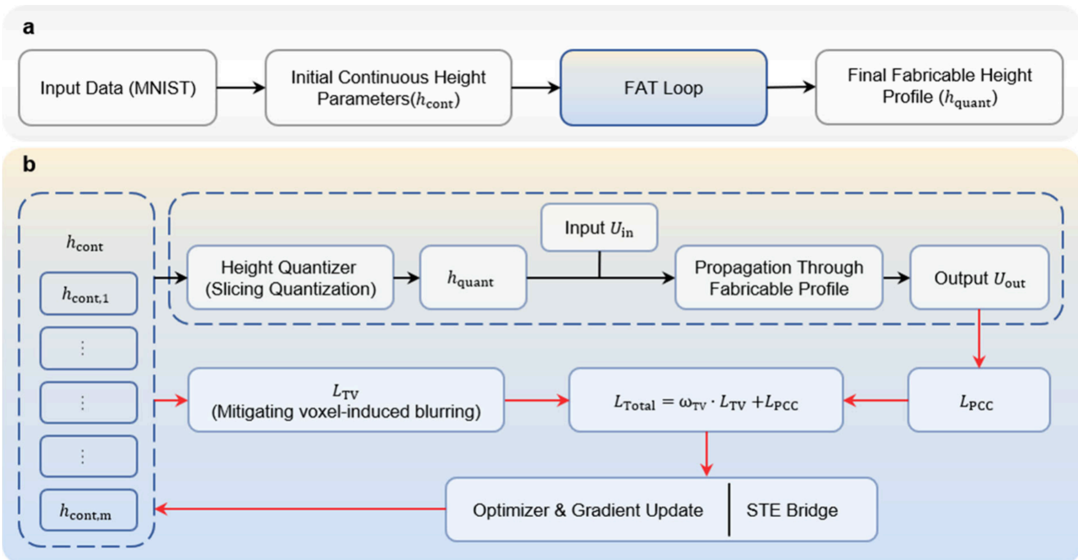


**Figure 3.** Architecture of the FAT framework. (a) FAT pipeline, mapping continuous height parameters to a final fabrication-compatible height profile. (b) Differentiable fabrication-aware forward model and optimization flow. Slicing-induced height quantization is incorporated in the forward propagation, while voxel-induced blurring is mitigated via a total variation loss $L_{TV}$. The global loss is defined as $L_{Total} = \omega_{TV} \times L_{TV} + L_{PCC}$, where $L_{PCC}$ denotes the Pearson correlation coefficient loss and $\omega_{TV}$ is a weighting factor that controls the relative contribution of the $L_{TV}$. Gradient backpropagation is enabled by a straight-through estimator (STE).

respectively. These perturbations are comparative surrogate models rather than printer-specific calibrations; accordingly, the analysis is intended to establish a sensitivity hierarchy within the examined ranges, rather than to assign the entire experimental discrepancy to a unique physical mechanism. Although the precise error magnitudes may vary with the fabrication system, photoresist, and exposure conditions, applying all perturbations to the same baseline provides a consistent basis for comparing their relative effects.

The results in Figure 2 reveal a clear difference in sensitivity among the four modeled perturbations. The ranges of voxel-induced blurring and slicing quantization were selected with reference to the effective focal volume and axial resolution of commercial TPP systems, while the axial-shrinkage and surface-roughness ranges were based on reported characterizations of the IP-DIP2 photoresist.[38] Voxel-induced blurring causes both classification accuracy and ECR to decrease progressively as the blur strength increases (Figure 2a). This degradation arises because the finite lateral extent of the


https://doi.org/10.1021/acs.nanolett.6c01607
Nano Lett. XXXX, XXX, XXX−XXX

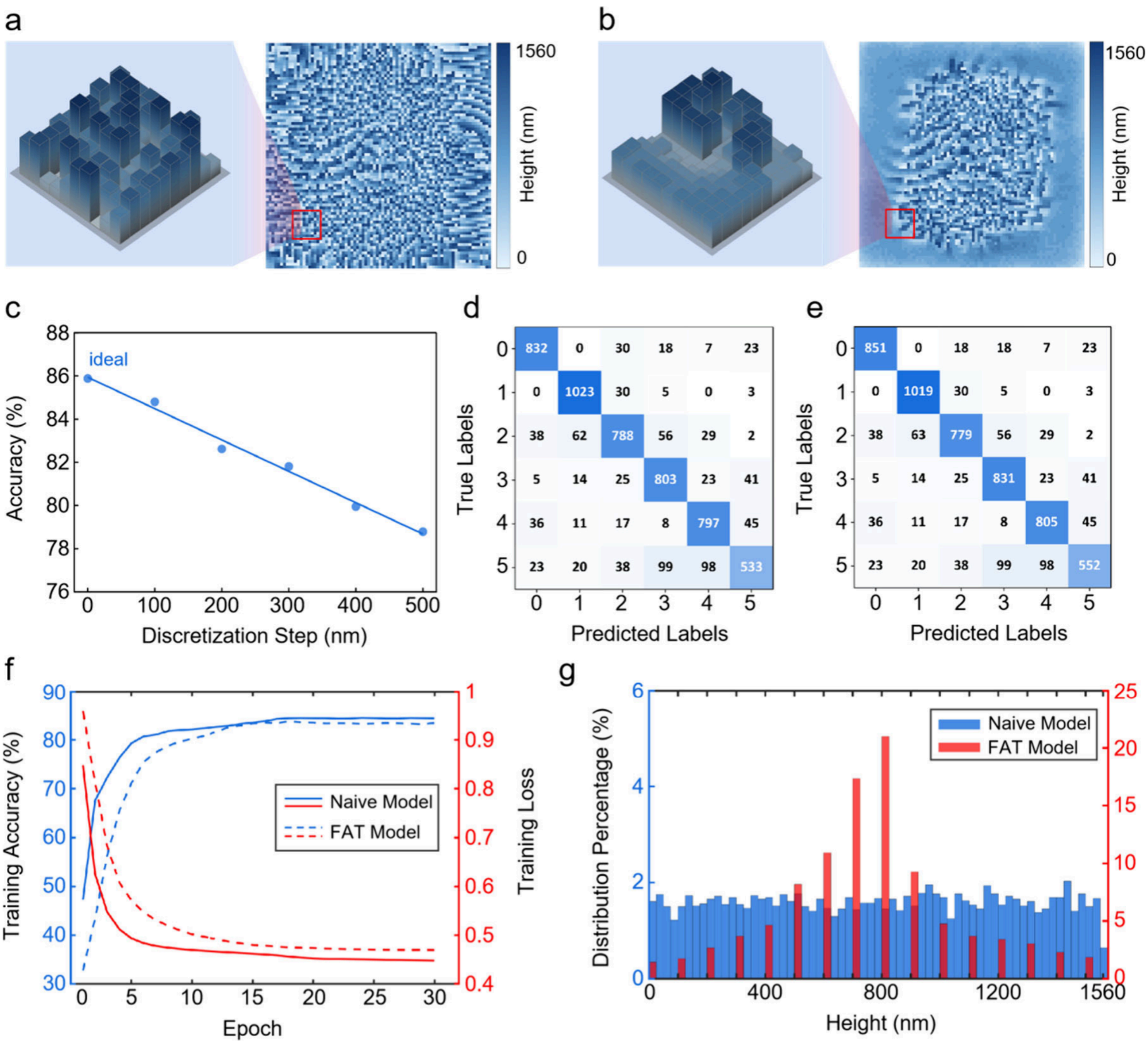


**Figure 4.** Comparative analysis of diffractive structures obtained via the Naive and the FAT models in simulation. (a, b) Height distributions of diffractive layers optimized using the Naive model (panel (a)) and the FAT model (panel (b)). (c) Regression trend of classification accuracy versus axial discretization step size. (d, e) Simulated classification confusion matrices for the Naive model (panel (d)) and the FAT model (panel (e)). (f) Training evolution of classification accuracy and loss over 30 epochs. (g) Statistical distributions of neuron height values.

writing voxel acts as a spatial low-pass filter on the designed height profile. Abrupt local height transitions and other high-spatial-frequency features are therefore smoothed during fabrication, preventing the fabricated structure from faithfully reproducing the phase modulation required by the optimized design. The resulting phase errors broaden the output features, increase the background intensity, and reduce the fraction of optical energy confined within the target detector region.

Slicing-induced height quantization produces a similarly pronounced deterioration (Figure 2b). As the number of available height levels decreases, the continuous height profile is represented by progressively coarser axial steps, increasing the difference between the optimized and fabrication-compatible phase profiles. This quantization error perturbs the relative phase accumulated across the diffractive layer and disrupts the interference conditions required to route light toward the correct detector region. Both classification accuracy and ECR consequently decrease as the axial discretization becomes coarser. The degradation becomes particularly pronounced below eight available height levels, corresponding to an axial slicing step of approximately 200 nm at $\lambda = 780$ nm.

By comparison, axial shrinkage and surface roughness produce smaller performance changes over the examined ranges (Figure 2c and 2d). Uniform axial shrinkage primarily rescales the overall modulation depth of the diffractive layer, while surface roughness introduces spatially localized random phase perturbations. Although both effects alter the optical response, their influence on classification accuracy and ECR is less pronounced than that of lateral smoothing and axial discretization under the conditions considered here. This result does not imply that shrinkage and roughness are negligible for every TPP process; rather, it identifies voxel-induced blurring


https://doi.org/10.1021/acs.nanolett.6c01607
Nano Lett. XXXX, XXX, XXX−XXX

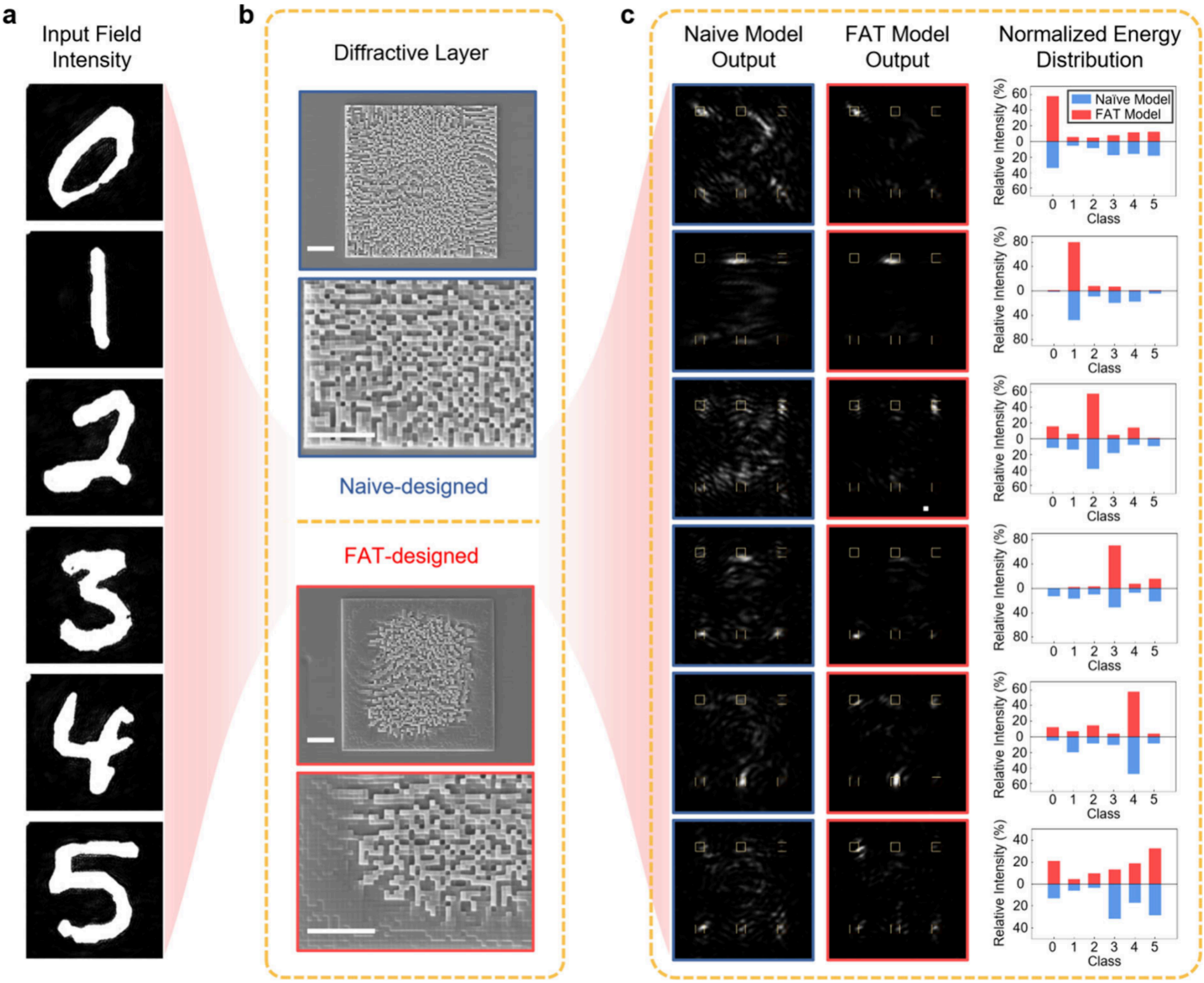


**Figure 5.** Experimental comparison of diffractive layers designed by the Naive and the FAT models. (a) Experimentally measured input optical intensity distributions for digit classes 0−5. (b) Scanning electron microscopy (SEM) images of fabricated diffractive layers, showing global morphology and local structural details. (c) Measured output intensity distributions under identical experimental conditions, with corresponding bar charts of normalized target-region intensities. Scale bar = 10 $\mu$m.

and slicing quantization as the dominant modeled sensitivities within the representative ranges examined in this study.

Collectively, the sensitivity analysis provides the physical basis for the FAT strategy. Slicing-induced height quantization is treated explicitly by enforcing fabrication-compatible discrete height levels during the forward propagation, whereas the effect of voxel-induced blurring is mitigated through total-variation regularization, which discourages abrupt local height changes and reduces reliance on features that are susceptible to smoothing by the finite writing voxel. FAT therefore targets the two fabrication constraints that most strongly degrade the Naive design, while avoiding unnecessary complexity associated with explicitly modeling every possible fabrication imperfection.

Guided by the analysis above, we formulate a FAT strategy that embeds the dominant fabrication constraints into the optimization of TPP-fabricated D2NNs. The overall pipeline is shown in Figure 3a. Accordingly, the forward model incorporates fabrication-aware modules that guide the optimized profiles toward compatibility with the manufacturing process. To account for the phase quantization inherently introduced by axial slicing, we explicitly enforce discretized height constraints in the forward propagation stage (Figure 3b). Specifically, the continuously optimized height parameters are projected onto a finite set of stepwise levels. These levels align with the prescribed slicing resolution. Both the optical field propagation and the subsequent loss evaluation are carried out based on this discretized representation. This approach ensures that the optimization objective reflects the performance of the physically realizable, quantized structure. While this hard quantization faithfully captures the physical discretization process, it introduces nondifferentiability that hinders gradient-based optimization. To circumvent this issue, we adopt a straight-through estimator (STE) during backpropagation. Within this framework, the quantization operation is treated as an identity mapping in the backward pass, allowing gradients to propagate through the discretization layer without compromising the physical consistency of the forward model.[39]




https://doi.org/10.1021/acs.nanolett.6c01607
Nano Lett. XXXX, XXX, XXX−XXX

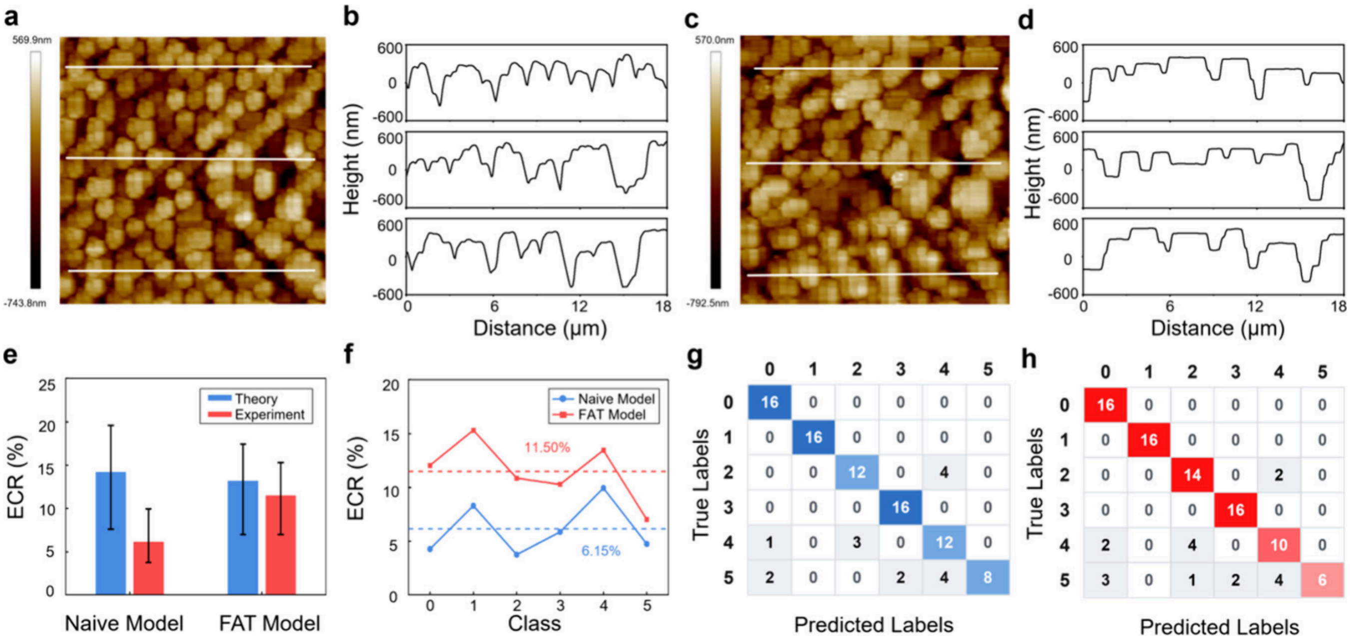


**Figure 6.** Structural characterization and optical performance of the fabricated diffractive layers. (a, c) AFM height maps of representative 20 $\mu$m × 20 $\mu$m regions of the Naive and FAT devices, respectively; white lines mark the positions of the profiles shown in (b, d), ordered from top to bottom. Height scales are indicated by the adjacent color bars. (e) Mean numerical and experimental ECRs calculated using the same fixed, class-balanced set of 96 inputs (16 per class). Error bars denote the standard deviation across the 96 samples. (f) Class-wise mean experimental ECRs. Dashed lines indicate the macro-averaged ECRs of 6.15% for Naive and 11.50% for FAT. (g, h) Experimental confusion matrices for the same 96 inputs, yielding classification accuracies of 83.3% (80/96) and 81.2% (78/96), respectively.

To alleviate voxel-induced blurring, we further introduce total-variation (TV) regularization to penalize excessive height differences between neighboring diffractive neurons. Large height differences between neurons create steep gradients and long sidewall regions. During layer-wise fabrication, the finite voxel size and exposure overlap lead to significant rounding of these sidewalls. Such rounding results in large deviations from the designed phase profile. By penalizing abrupt height variations, TV regularization promotes smooth transitions and preserves the intended phase modulation. Together with discretized height constraints, this regularization restricts the optimization to fabrication-compatible phase profiles.

The TV weight was selected through a validation-set sweep from zero to $1 \times 10^{-4}$, with all other optical and training settings held fixed (Figure S7). We adopted $\omega_{TV} = 3 \times 10^{-5}$ as a balance between fabrication compatibility and numerical performance: the mean neighbor-to-neighbor height variation decreased from approximately 493 to 258 nm, while the validation accuracy changed only from 85.8% to 84.7%. Larger weights further smoothed the profile but produced a more pronounced loss of accuracy. Consistent with this selection, the final FAT height map exhibits 32% lower absolute spectral power above 0.40 cycles $\mu m^{-1}$ than the Naive design, whereas the fraction of power in this band decreases by a more modest 8%, because the total spectral power is also reduced (Figure S8).

Figure 4a and 4b directly compare the optimized height maps obtained using the Naive and FAT models. The Naive design contains dense neuron-to-neuron height variations and numerous isolated high-gradient features, whereas the FAT design exhibits broader, more spatially connected regions with smoother local transitions. We next determine an optimal slicing step size that balances simulated performance with fabrication feasibility. Because accuracy improves as the slicing step decreases (Figure 4c), we adopted a 100 nm step, corresponding to the 16 height levels used for fabrication. Figure 4d and 4e present the class-resolved numerical confusion matrices, while the training histories in Figure 4f show stable convergence of both accuracy and loss over 30 epochs. The neuron-height histograms in Figure 4g further illustrate how FAT reshapes the design: the Naive profile remains approximately continuous, whereas the FAT profile concentrates around the enforced levels and relies less on extreme heights. Relative to the Naive design, FAT reduces the mean neighbor-to-neighbor height variation by 48% and the absolute spectral power above 0.40 cycles $\mu m^{-1}$ by 32% (Figure S8). Because the total spectral power also decreases, the fraction of power in this band is reduced more modestly, to 0.92 times the Naive value. Meanwhile, the numerical test accuracy decreases only slightly, from 85.8% to 84.8% (Figure 4d and 4e). Thus, FAT substantially improves the fabrication compatibility of the optimized height profile while largely preserving its ideal numerical performance, with only a one-percentage-point reduction in test accuracy.

To determine whether this simulation-level robustness translates into physical performance gains, we next carry out experimental validation by fabricating single-layer diffractive phase masks designed by the Naive and the FAT models. These masks are produced using a commercial TPP system and characterized under identical conditions (see the Supporting Information for experimental details). Input digit patterns are encoded onto the incident optical field via amplitude modulation using a spatial light modulator (SLM) and relayed to the diffractive layer through a 4f imaging system. A CCD camera records the resulting output intensity distributions at the detector plane, located at a design propagation distance of 100 $\mu$m. Figure S1 provides a schematic of the experimental optical setup. Unless otherwise specified, all measurements are conducted at $\lambda$ = 780 nm with identical acquisition parameters and post-processing procedures to ensure a fair comparison between the two training strategies.

Representative experimental results for different input digits are shown in Figure 5. For the Naive-designed diffractive layer, the measured output fields exhibit broadened focal spots and elevated background intensity. This indicates substantial optical energy leakage into nontarget detector regions, reflecting the intrinsic limitations of the TPP fabrication process in reproducing high-spatial-frequency phase features. In contrast, the FAT-fabricated diffractive layer produces well-confined focal spots. Background intensity is strongly suppressed, and optical energy is preferentially routed toward the intended channels. This results in improved contrast and signal-to-noise at the detector plane.

The normalized target-region intensities in Figure 5 further quantify this behavior. For digit "0", the FAT-designed diffractive layer yields a dominant response in the target detector region with clear separation from nontarget responses. Conversely, the Naive counterpart shows markedly reduced contrast. Similar trends are consistently observed across the other digit classes, demonstrating that the FAT enhances interclass intensity separation and stabilizes optical decision making in the fabricated system.

Figure 5 presents representative measured output fields, whereas the quantitative structural and optical comparisons are summarized in Figure 6 using the complete experimental dataset. The AFM height maps in Figure 6a and 6c reveal distinct morphological characteristics of representative regions from the two fabricated devices. The Naive device exhibits more pronounced local height contrast, with numerous spatially isolated protrusions and depressions, resulting in a relatively fragmented surface morphology and larger local peak-to-valley variations. In comparison, the FAT device contains more laterally connected plateau-like regions, with smoother transitions between adjacent height levels and fewer isolated features. This difference is further supported by the corresponding line profiles in Figure 6b and 6d. The Naive profiles contain frequent irregular peaks and valleys with rounded and nonuniform feature widths, whereas the FAT profiles exhibit flatter plateaus, more clearly defined step-like transitions, and more regular quasi-rectangular features. These observations indicate that FAT suppresses excessive local height fluctuations and promotes a more ordered, terrace-like morphology, consistent with its lower height variation and reduced high-spatial-frequency content (Figure S8).

To quantitatively evaluate optical inference, we calculated the ECR for a fixed, class-balanced set of 96 inputs, with 16 samples from each digit class measured on both devices. For each input, ECR was defined as the optical energy within the detector assigned to the true class divided by the total energy within a fixed output region. The same detector regions and analysis procedure were used for the numerical and experimental data, and experimental ECRs were calculated from linear CCD intensities. As shown in Figure 6e, the Naive mean ECR decreases from 14.21% in simulation to 6.15% in experiment. By contrast, the FAT mean ECR decreases only from 13.19% to 11.50%. The corresponding simulation-to-experiment gap is therefore reduced from 8.06 to 1.69 percentage points, representing a 79.03% reduction. FAT also achieves a higher mean experimental ECR in every digit class (Figure 6f), demonstrating more faithful routing of optical energy after fabrication.

The experimental confusion matrices provide a direct evaluation of the inference performance of the fabricated devices (Figure 6g and 6h). Using the same fixed, class-balanced set of 96 inputs, the Naive and FAT devices correctly classify 80 and 78 samples, yielding experimental accuracies of 83.3% and 81.2%, respectively. This tradeoff is consistent with the numerical results, demonstrating that FAT sacrifices only a small degree of classification accuracy while substantially improving the fidelity of optical-energy routing in the fabricated device.

This improvement arises from incorporating the dominant TPP constraints directly into optimization. Conventional training may produce continuous height profiles with abrupt variations that are difficult to reproduce because of axial slicing and the finite writing voxel. FAT instead enforces fabrication-compatible height levels during forward propagation and applies TV regularization to suppress excessive differences between neighboring neurons. The resulting profiles rely less on features susceptible to discretization and voxel-induced rounding, allowing the fabricated layer to preserve its intended phase modulation more faithfully. FAT does not overcome the physical resolution limits of TPP; it redirects the optimization toward features that can be reliably fabricated.

A residual discrepancy between simulation and experiment nevertheless remains. Possible contributors include nonuniform polymerization and unmodeled geometric deviations, residual wavefront and alignment errors, detector noise, and the limited routing capacity of a single diffractive layer. Figure S9 shows comparable relative sensitivities of the Naive and FAT designs to the examined lateral and axial offsets. Because these error sources were not independently measured, their individual contributions cannot yet be determined.

Although demonstrated here using a single-layer D2NN, the fabrication-aware framework can, in principle, be extended to multilayer architectures, other nanofabrication processes, and wavefront-engineering tasks such as holography and beam shaping, provided that the dominant process constraints can be modeled differentiably. Future work could incorporate exposure-dependent polymerization, shrinkage, and structural deformation through physics-based or hybrid data-driven surrogates. Evaluations under interlayer misalignment, partially coherent illumination, and larger optical systems will also be important for practical deployment.

In summary, we developed a fabrication-aware training (FAT) framework for TPP-fabricated D2NNs. Sensitivity analysis identified voxel-induced blurring and slicing-induced height quantization as the dominant fabrication constraints, which were addressed through total-variation regularization and differentiable height quantization, respectively. The resulting FAT design exhibited reduced local height variation and high-spatial-frequency content while retaining a simulated classification accuracy of 84.8%. AFM measurements further confirmed smoother, more terrace-like fabricated profiles. For a fixed, class-balanced set of 96 handwritten-digit inputs, FAT increased the mean experimental ECR from 6.15% to 11.50% and reduced the simulation-to-experiment gap by 79.03%, with only a modest decrease in experimental classification accuracy from 83.3% to 81.2%. These results demonstrate that explicitly embedding fabrication constraints into optimization improves the physical fidelity of diffractive devices and provides a general




https://doi.org/10.1021/acs.nanolett.6c01607
Nano Lett. XXXX, XXX, XXX−XXX

route toward robust nanofabricated optical computing and wavefront engineering.

## ■ ASSOCIATED CONTENT

### Supporting Information

The Supporting Information is available free of charge at https://pubs.acs.org/doi/10.1021/acs.nanolett.6c01607.

> Mathematical modeling of fabrication constraints; additional computational, fabrication, and experimental details;TV-regularization-weight sensitivity; spatial-frequency analysis of the Naive and FAT height maps; schematic of the experimental optical characterization setup; simulated effects of voxel-induced blurring, phase quantization, axial shrinkage, and surface roughness; simulated results under combined fabrication-induced errors; and lateral and axial alignment-tolerance analysis (PDF)

## ■ AUTHOR INFORMATION

### Corresponding Author

**Yanlei Hu** − *State Key Laboratory of Optoelectronic Information Acquisition and Protection Technology, Department of Precision Machinery and Precision Instrumentation, University of Science and Technology of China, Hefei 230027, China;* orcid.org/0000-0003-1964-0043; Email: huyl@ustc.edu.cn

### Authors

**Jiale Yao** − *State Key Laboratory of Optoelectronic Information Acquisition and Protection Technology, Department of Precision Machinery and Precision Instrumentation, University of Science and Technology of China, Hefei 230027, China*

**Jiabin Bi** − *State Key Laboratory of Optoelectronic Information Acquisition and Protection Technology, Department of Precision Machinery and Precision Instrumentation, University of Science and Technology of China, Hefei 230027, China*

**Yuhang Xue** − *State Key Laboratory of Optoelectronic Information Acquisition and Protection Technology, Department of Precision Machinery and Precision Instrumentation, University of Science and Technology of China, Hefei 230027, China*

**Liqun Xu** − *State Key Laboratory of Optoelectronic Information Acquisition and Protection Technology, Department of Precision Machinery and Precision Instrumentation, University of Science and Technology of China, Hefei 230027, China; Circuit Fabology Microelectronics Equipment Co., Ltd., Hefei 230088, China*

**Zhaohui Ye** − *State Key Laboratory of Optoelectronic Information Acquisition and Protection Technology, Department of Precision Machinery and Precision Instrumentation, University of Science and Technology of China, Hefei 230027, China*

**Haowen Liu** − *State Key Laboratory of Optoelectronic Information Acquisition and Protection Technology, Department of Precision Machinery and Precision Instrumentation, University of Science and Technology of China, Hefei 230027, China*

**Bowen Chen** − *State Key Laboratory of Optoelectronic Information Acquisition and Protection Technology, Department of Precision Machinery and Precision Instrumentation, University of Science and Technology of China, Hefei 230027, China*

**Jincheng Ni** − *State Key Laboratory of Optoelectronic Information Acquisition and Protection Technology, Department of Precision Machinery and Precision Instrumentation, University of Science and Technology of China, Hefei 230027, China*

**Jiawen Li** − *State Key Laboratory of Optoelectronic Information Acquisition and Protection Technology, Department of Precision Machinery and Precision Instrumentation, University of Science and Technology of China, Hefei 230027, China;* orcid.org/0000-0003-3950-6212

**Dong Wu** − *State Key Laboratory of Optoelectronic Information Acquisition and Protection Technology, Department of Precision Machinery and Precision Instrumentation, University of Science and Technology of China, Hefei 230027, China;* orcid.org/0000-0003-0623-1515

Complete contact information is available at: https://pubs.acs.org/10.1021/acs.nanolett.6c01607

### Author Contributions

[∇]Authors J.Y. and J.B. contributed equally to this work. The manuscript was written through contributions of all authors. All authors have given approval to the final version of the manuscript.

### Funding

National Key Research and Development Program of China (No. 2024YFB4610700), National Natural Science Foundation of China (Nos. 52375582, 62575274, and 62475252); CAS Project for Young Scientists in Basic Research (No. YSBR-049); Fundamental Research Funds for the Central Universities (WK2090000088 and WK2090000081); "University of Science and Technology of China-Southwest University of Science and Technology Counterpart Cooperation and Development Joint Fund" (24LHJJ08).

### Notes

The authors declare no competing financial interest.

## ■ ACKNOWLEDGMENTS

We acknowledge the Experimental Center of Engineering and Material Sciences at USTC for the fabrication and measuring of samples. This work was partly carried out at the USTC Center for Micro and Nanoscale Research and Fabrication.

## ■ REFERENCES

(1) Mehonic, A.; Kenyon, A. J. Brain-Inspired Computing Needs a Master Plan. *Nature* **2022**, *604* (7905), 255−260.

(2) Marković, D.; Mizrahi, A.; Querlioz, D.; Grollier, J. Physics for Neuromorphic Computing. *Nature Reviews Physics* **2020**, *2*, 499−510.

(3) Roy, K.; Kosta, A.; Sharma, T.; et al. Breaking the Memory Wall: Next-Generation Artificial Intelligence Hardware. *Frontiers in Science* **2025**, *3*, 1611658.

(4) Maslej, N.; Fattorini, L.; Perrault, R.et al.Artificial Intelligence Index Report 2025. *arXiv Preprints* **2025**, arXiv:2504.07139, DOI: 10.48550/arXiv.2504.07139.

(5) Fu, T.; Zhang, J.; Sun, R.; et al. Optical Neural Networks: Progress and Challenges. *Light: Science & Applications* **2024**, *13* (1), 263.

(6) Shastri, B. J.; Tait, A. N.; Ferreira de Lima, T.; et al. Photonics for Artificial Intelligence and Neuromorphic Computing. *Nat. Photonics* **2021**, *15* (2), 102−114.
(7) Liu, J.; Wu, Q.; Sui, X.; et al. Research Progress in Optical Neural Networks: Theory, Applications and Developments. *PhotoniX* **2021**, *2* (1), 5.
(8) Liao, K.; Dai, T.; Yan, Q.; Hu, X.; Gong, Q. Integrated Photonic Neural Networks: Opportunities and Challenges. *ACS Photonics* **2023**, *10* (7), 2001−2010.
(9) Bandyopadhyay, S.; Sludds, A.; Krastanov, S.; et al. Single-Chip Photonic Deep Neural Network with Forward-Only Training. *Nat. Photonics* **2024**, *18* (12), 1335−1343.
(10) Lin, X.; Rivenson, Y.; Yardimci, N. T.; et al. All-Optical Machine Learning Using Diffractive Deep Neural Networks. *Science* **2018**, *361* (6406), 1004−1008.
(11) Chen, H.; Lou, S.; Wang, Q.; Huang, P.; Duan, H.; Hu, Y. Diffractive Deep Neural Networks: Theories, Optimization, and Applications. *Applied Physics Reviews* **2024**, *11* (2), No. 021332.
(12) Hu, J.; Mengu, D.; Tzarouchis, D. C.; Edwards, B.; Engheta, N.; Ozcan, A. Diffractive Optical Computing in Free Space. *Nat. Commun.* **2024**, *15* (1), 1525.
(13) He, C.; Zhao, D.; Fan, F.; Zhou, H.; Li, X.; Li, Y.; Li, J.; Dong, F.; Miao, Y.-X.; Wang, Y.; Huang, L. Pluggable Multitask Diffractive Neural Networks Based on Cascaded Metasurfaces. *Opto-Electron. Adv.* **2024**, *7* (2), No. 230005.
(14) Li, J.; Luo, Y.; Ozcan, A.; et al. Spectrally Encoded Single-Pixel Machine Vision Using Diffractive Networks. *Science Advances* **2021**, *7* (13), No. eabd7690.
(15) Luo, Y.; Mengu, D.; Yardimci, N. T.; Rivenson, Y.; Veli, M.; Jarrahi, M.; Ozcan, A. Design of Task-Specific Optical Systems Using Broadband Diffractive Neural Networks. *Light: Sci. Appl.* **2019**, *8* (1), 112.
(16) Veli, M.; Mengu, D.; Yardimci, N. T.; Luo, Y.; Li, J.; Rivenson, Y.; Jarrahi, M.; Ozcan, A. Terahertz Pulse Shaping Using Diffractive Surfaces. *Nat. Commun.* **2021**, *12* (1), 37.
(17) Li, J.; Li, X.; Yardimci, N. T.; Hu, J.; Li, Y.; Chen, J.; Hung, Y.-C.; Jarrahi, M.; Ozcan, A. Rapid Sensing of Hidden Objects and Defects Using a Single-Pixel Diffractive Terahertz Sensor. *Nat. Commun.* **2023**, *14* (1), 6791.
(18) Liao, D.; Chan, K. F.; Chan, C. H.; Zhang, Q.; Wang, H. All-Optical Diffractive Neural Networked Terahertz Hologram. *Opt. Lett.* **2020**, *45* (10), 2906−2909.
(19) Goi, E.; Chen, X.; Zhang, Q.; Cumming, B. P.; Schoenhardt, S.; Luan, H.; Gu, M. Nanoprinted High-Neuron-Density Optical Linear Perceptrons Performing Near-Infrared Inference on a CMOS Chip. *Light Sci. Appl.* **2021**, *10* (1), 40.
(20) Chen, H.; Feng, J.; Jiang, M.; Wang, Y.; Lin, J.; Tan, J.; Jin, P. Diffractive Deep Neural Networks at Visible Wavelengths. *Engineering* **2021**, *7* (10), 1483−1491.
(21) Bai, B.; Wei, H.; Yang, X.; Gan, T.; Mengu, D.; Jarrahi, M.; Ozcan, A. Data-Class-Specific All-Optical Transformations and Encryption. *Adv. Mater.* **2023**, *35* (31), No. 2212091.
(22) Yu, H.; Huang, Z.; Lamon, S.; et al. All-optical image transportation through a multimode fibre using a miniaturized diffractive neural network on the distal facet. *Nat. Photonics* **2025**, *19* (5), 486−493.
(23) Wang, H.; Zhang, W.; Ladika, D.; et al. Two-Photon Polymerization Lithography for Optics and Photonics: Fundamentals, Materials, Technologies, and Applications. *Adv. Funct. Mater.* **2023**, *33* (39), No. 2214211.
(24) O'Halloran, S.; Pandit, A.; Heise, A.; Kellett, A. Two-Photon Polymerization: Fundamentals, Materials, and Chemical Modification Strategies. *Advanced Science* **2023**, *10* (7), No. 2204072.
(25) Gu, Z.; Ma, Q.; Gao, X.; You, J. W.; Cui, T. J. Classification of Metal Handwritten Digits Based on Microwave Diffractive Deep Neural Network. *Advanced Optical Materials* **2024**, *12* (7), No. 2301938.
(26) Goi, E.; Schoenhardt, S.; Gu, M. Direct retrieval of Zernike-based pupil functions using integrated diffractive deep neural networks. *Nat. Commun.* **2022**, *13* (1), 7531.
(27) Boudene, I.; Bougdid, Y. Two-photon polymerization-assisted 3D laser nanoprinting: from fundamentals to modern applications. *Journal of Materials Chemistry C* **2025**, *13* (36), 18597−18630.
(28) Wang, H.; Pan, C. F.; Li, C.; et al. Two-photon polymerization lithography for imaging optics. *International Journal of Extreme Manufacturing* **2024**, *6* (4), No. 042002.
(29) Wang, H.; Wang, H.; Zhang, W.; Yang, J. K. W. Toward Near-Perfect Diffractive Optical Elements via Nanoscale 3D Printing. *ACS Nano* **2020**, *14* (8), 10452−10461.
(30) Pan, C. F.; Wang, H.; Wang, H.; et al. 3D-Printed Multilayer Structures for High-Numerical-Aperture Achromatic Metalenses. *Science Advances* **2023**, *9* (51), No. eadj9262.
(31) Wu, B.; Wang, H.; Pan, C.-F.; et al. Wide Angle 3D Imaging without Distortions. *Laser & Photonics Reviews* **2026**, *20* (5), No. e01827.
(32) Mengu, D.; Zhao, Y.; Yardimci, N. T.; et al. Misalignment resilient diffractive optical networks. *Nanophotonics* **2018**, *9* (13), 4207−4219.
(33) Wang, Q.; Yu, H.; Huang, Z.; Gu, M.; Zhang, Q. Two-photon nanolithography of micrometer scale diffractive neural network with cubical diffraction neurons at the visible wavelength. *Chinese Optics Letters* **2024**, *22* (10), No. 102201.
(34) Wright, L. G.; Onodera, T.; Stein, M. M.; et al. Deep physical neural networks trained with backpropagation. *Nature* **2022**, *601* (7894), 549−555.
(35) Spall, J.; Guo, X.; Lvovsky, A. I. Hybrid training of optical neural networks. *Optica* **2022**, *9* (7), 803−811.
(36) Pai, S.; Sun, Z.; Hughes, T. W.; et al. Experimentally realized in situ backpropagation for deep learning in photonic neural networks. *Science* **2023**, *380* (6643), 398−404.
(37) Yuan, X.; Wang, Y.; Xu, Z.; et al. Training large-scale optoelectronic neural networks with dual-neuron optical-artificial learning. *Nat. Commun.* **2023**, *14* (1), 7110.
(38) Bauer, J.; Izard, A. G.; Zhang, Y.; Baldacchini, T.; Valdevit, L. Thermal post-curing as an efficient strategy to eliminate process parameter sensitivity in the mechanical properties of two-photon polymerized materials. *Opt. Express* **2020**, *28* (14), 20362−20371.
(39) Tang, Z.; Luo, L.; Xie, B.; et al. Automatic sparse connectivity learning for neural networks. *IEEE Transactions on Neural Networks and Learning Systems* **2023**, *34* (10), 7350−7364.




https://doi.org/10.1021/acs.nanolett.6c01607
*Nano Lett.* XXXX, XXX, XXX−XXX